Electronic Supplementary Information

Hierarchically interconnected porous scaffolds for phase change materials with improved thermal conductivity and efficient solar-to-electric energy conversion

Jie Yang, Peng Yu, Li-Sheng Tang, Rui-Ying Bao, Zheng-Ying Liu, Ming-Bo Yang, Wei Yang*

College of Polymer Science and Engineering, Sichuan University, State Key Laboratory of Polymer Materials Engineering, Chengdu, 610065, Sichuan, People's Republic of China.

Experimental section

Materials

The original graphite (200 mesh, purity > 99.9%) was purchased from Laixi Nanshu Fada Graphite Company (Qingdao, China). BN (10~15 um, purity > 99%) and PEG (Mn = 10 000) were provided by Qinhuangdao Eno High-Tech Material Development CO., LTD. and Aladdin Reagent (Shanghai, China), respectively. The reagents, including concentrated sulfuric acid (H_2SO_4), potassium permanganate ($KMnO_4$), potassium persulfate ($K_2S_2O_8$), phosphorus pentoxide (P_2O_5), hydrogen peroxide (H_2O_2), hydrochloric acid (HCl) and absolute alcohol were purchased from Haihong Chemical Reagents Company (Chengdu, China) and of analytical grade.

Characterization

The SEM images of 3D porous scaffolds and composite PCMs were taken by using a field-emission SEM instrument (JEOL JSM-5900LV, Japan) with 20 kV or 10 kV accelerating voltage. The elemental mapping of 3D porous scaffolds was obtained by using the SEM (Quanta 250, FEI Company, USA). The XRD patterns in the range of diffraction angle 2θ = 5–60° at a scanning speed of 10 ° min^{-1} were performed by a Rigaku UltimaIV diffractometer (Rigaku, Japan) with Cu Kα radiation (λ = 0.15406 nm). UV-vis-NIR absorption spectrum (UV-vis-NIR spectrophotometer, UV3600, Shimadzu, Japan) of GO was conducted to confirm its chemical structure. FTIR spectroscopy patterns over the wavenumber range of 4000–400 cm^{-1} were performed

Corresponding author. Tel.: + 86 28 8546 0130; fax: + 86 28 8546 0130.

E-mail address: weiyang@scu.edu.cn (W Yang)

using a Nicolet 6700 FTIR spectrometer (Nicolet Instrument Company, USA) with a resolution of 4 cm^{-1} in the transmission mode. Thermal gravimetric analysis (TGA, TG209F1, Netzsch, Germany) was applied to determine the content of BN in the composite PCMs. The temperature was increased from 30 to 700 °C at the rate of 10 °C min^{-1} in the air atmosphere. The thermal properties (phase change temperature, phase change enthalpy and cycling stability) of pure PEG and the composite PCMs were characterized by differential scanning calorimetry (DSC, TA Q20 instrument, USA) with a heating/cooling rate of 10 °C min^{-1} in a highly purified nitrogen atmosphere. The thermal conductivity and heat transfer were measured through a transient plane heat source method (Hot Disk Thermal Constant Analyzer, TPS 2500, Hot Disk AB Company, Sweden) at room temperature (ca. 25 °C) and an infrared camera (Ti27, Fluke, USA), respectively. A light-to-electric energy conversion test was performed using a CEL-HXUV300 xenon lamp with an AM 1.5 filter and a commercial Seebeck thermoelectric device. The samples were placed on the surface of thermoelectric device to serve as heat source, while tap water was used as cold source. The real-time current (*I*) was recorded using a Keithley electrometer (2400, Cleveland, Ohio, USA) under the simulated sunlight irradiation of 800 mW cm^{-2} verified via a CEL-NP2000 optical power meter (CEAULIGHT, China).

Results

Fig. S1a shows that BN sheets present smoother surface and smaller size. From the XRD pattern of BN (**Fig. S1**b), the typical diffraction peaks appear at ca. 26.54° and ca. 41.44° corresponding to (002) and (100) planes of BN crystal, respectively. The FTIR spectrum of BN (**Fig. S1**c) shows two distinct peaks at 1374 cm^{-1} and 814 cm^{-1} which can be attributed to the B-N stretching and the B-N bending respectively. Compared with BN, GO sheets in **Fig. S2**a exhibit wrinkled surface textures with curling edges. The XRD pattern (**Fig. S2**b) and FTIR spectrum (**Fig. S2**d) of both original graphite and GO show significant differences. The XRD pattern of GO indicates that the interlayer spacing GO increases dramatically due to the attachment of various oxygen-containing functional groups on the C–C basal planes. Also, corresponding characteristic peaks emerge in the FTIR spectrum, such as C=O, C-OH and C-O. The UV-vis-NIR absorption spectrum of GO presents a strong absorption peak at ~ 229 nm and a weak shoulder peak at ~ 300 nm owing to π- π^* transitions of

the conjugation domains and n-π* transitions of the carbonyl groups respectively, as shown in **Fig. S2**c.

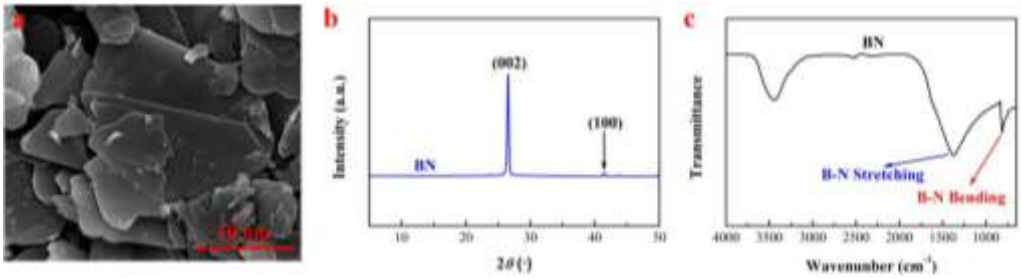

Fig. S1 (a) SEM image, (b) XRD pattern and (c) FTIR spectrum of BN.

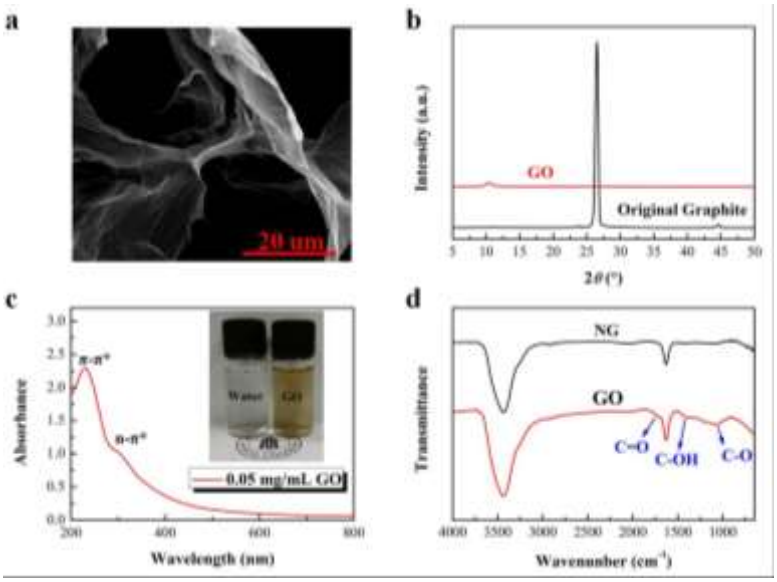

Fig. S2 (a) SEM image, (b) XRD pattern, (c) UV-vis-NIR absorption spectrum and (d) FTIR spectrum of GO.

Fig. S3 intuitively shows that the digital photographs of porous scaffolds present layered (hierarchial) structure along the ice crystal growth direction in the macro scale.

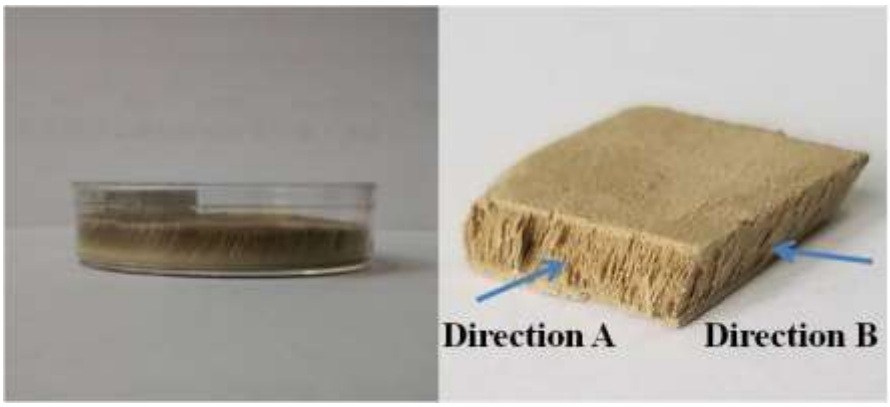

Fig. S3 Digital photographs of hierarchical porous scaffolds.

The elemental mapping provides evidence that there is a dual network in the porous scaffolds, as shown in **Fig. S4.** The C and N elements represent GO and BN,

respectively. Obviously, both GO and BN present hierarchically ordered structure in the whole view.

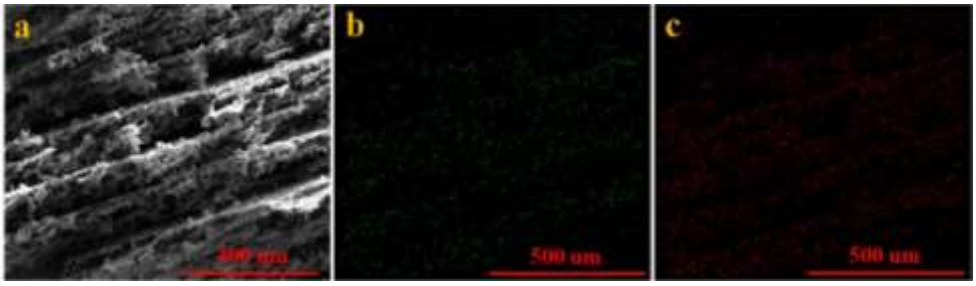

Fig. S4 (a) SEM image, (b) C (green) elemental mapping and (c) N (red) elemental mapping of the porous scaffolds.

The parallel (from direction B) cross-sectional SEM images of hierarchical porous scaffolds shown in **Fig. S5** exhibit a completely different structure, like "walls", compared with the perpendicular (from direction A) cross-sectional SEM images.

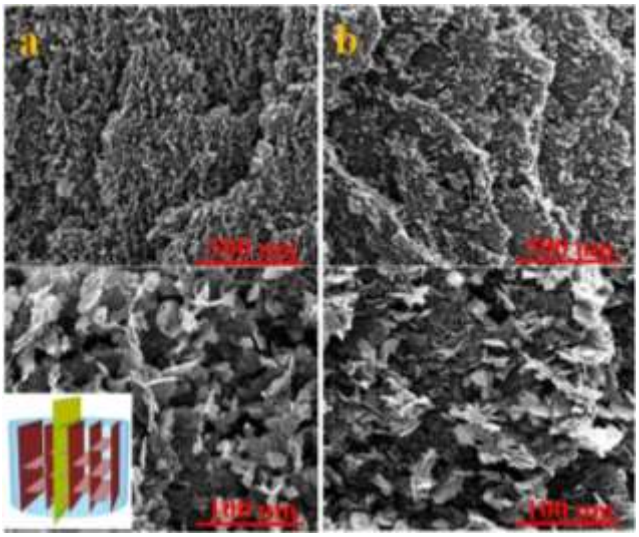

Fig. S5 The parallel (parallel to the lamellae from direction B) cross-sectional SEM images of (a) A2 and (b) A4.

The size of the interlayer space (*d*) and the thickness of layer (*t*) is measured and counted by Image-Pro Plus, and the results are shown in **Fig. S6**.

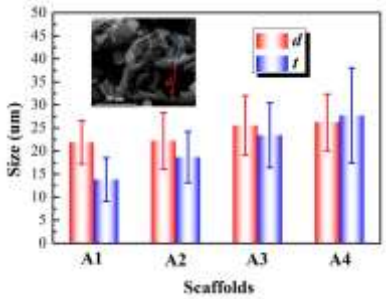

Fig. S6 The size of *d* and *t* of the scaffolds.

Fig. S7 shows the SEM images of pure PEG and the composite PCMs (C3), where the red arrows represent the hierarchical structure (thermally conductive pathway) constructed by BN in the composites. Compared with pure PEG, C3 exhibits rougher fracture surface owing to the introduction of GO and BN.

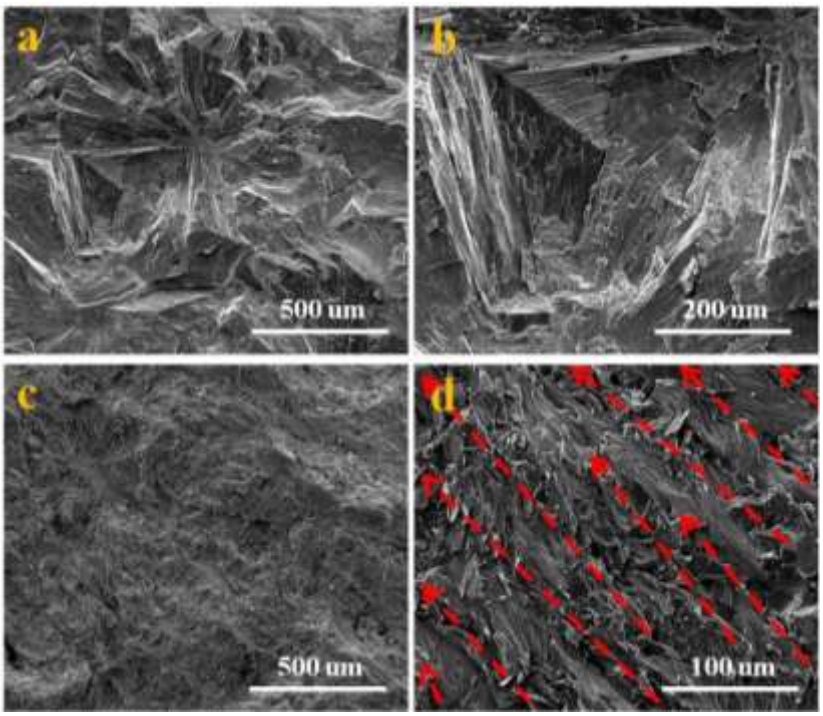

Fig. S7 SEM images of fractured surfaces of (a) and (b) PEG, (c) and (d) the composite PCMs.

Fig. S8 shows that PEG and GO experience weight loss completely up to 700 °C in the air atmosphere, while pristine BN exhibits high thermal stability with a negligible decomposition in the whole process.

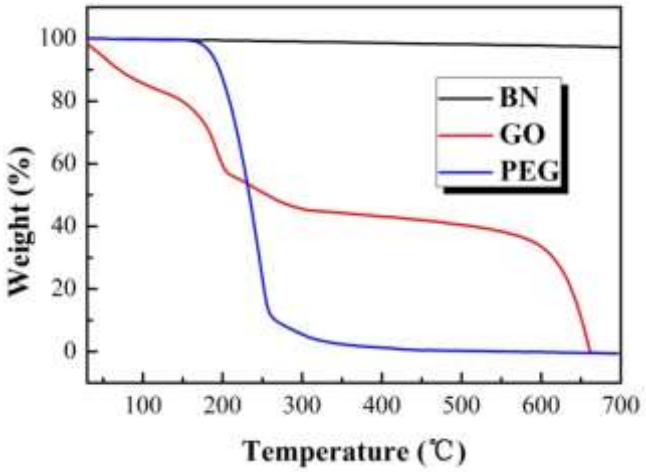

Fig. S8 TGA curves of BN, GO and PEG.

The phase change temperatures and phase change enthalpies of C4 after 100 heating and cooling cycles are presented in **Table S1**. Only a slight change in the thermal properties is observed over 100 cycles.

Table S1 Thermal properties of C4 after 100 heating and cooling cycles.

Cycling number	T_{cp} (°C)	ΔH_{cc} (J g^{-1})	T_{mp} (°C)	ΔH_{mc} (J g^{-1})
1	42.8	129.3	65.2	136.6
51	44.4	130.7	65.2	137.2
101	44.0	130.4	64.7	137.4

The temperature distribution images at 13, 38, 67 and 119 s and at 8, 21, 33 and 54 s are shown in **Fig. 9** for the pure PEG and C4 composite PCM while heating and cooling, respectively. During heating, the temperature increase of C4 composite PCM is much faster compared with that of pure PEG, indicating that the composite PCM exhibits much better thermal response behavior due to its higher thermal conductivity. As expected, the temperature decrease of C4 composite PCM is much faster than that of pure PEG.

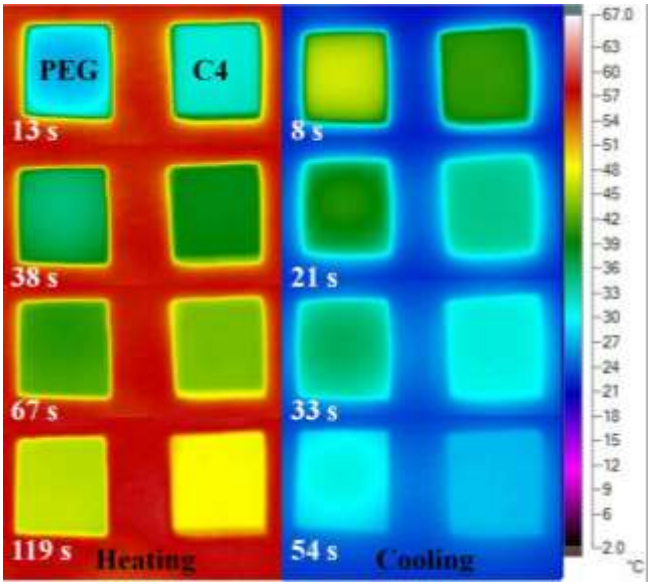

Fig. S9 Thermal transport evolution of PEG and C4 during heating and cooling.

Fig. S10a intuitively shows that GO nanosheets overlap with each other to form a 3D supporting network (including the walls and bridges) and BN particles are aggregated along the network structure of GO to develop thermally conductive pathway. Moreover, the elemental mapping of 3D porous scaffolds provides additional

evidence that the bridge is composed of a small amount of GO and BN, as shown in **Fig. S10**b, c and d.

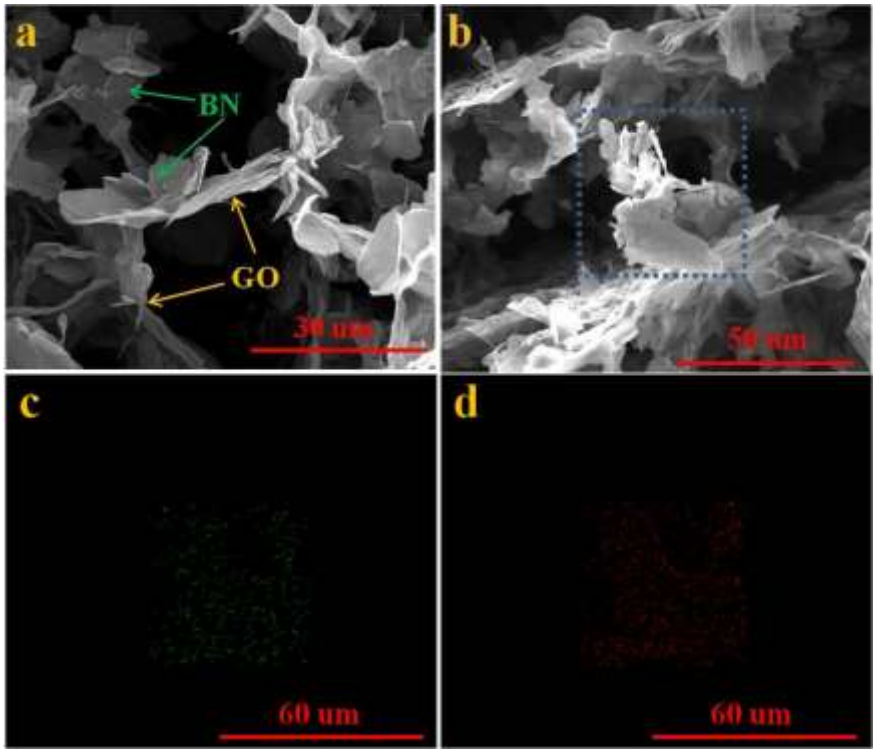

Fig. S10 (a)-(b)SEM images of the porous scaffolds, (c) C (green) elemental mapping and (d) N (red) elemental mapping of the area marked by blue square in Fig. S10b.

The intermolecular hydrogen bonding interactions between PEG and GO are proved by the FTIR spectra. The most absorption peaks of the functional groups of PEG emerge with only a slight shift of peak positions in C2 and C4, as shown in **Fig. S11**. For example, the peak of C–O groups in the composite PCMs shifts to lower wavenumbers compared with pure PEG.

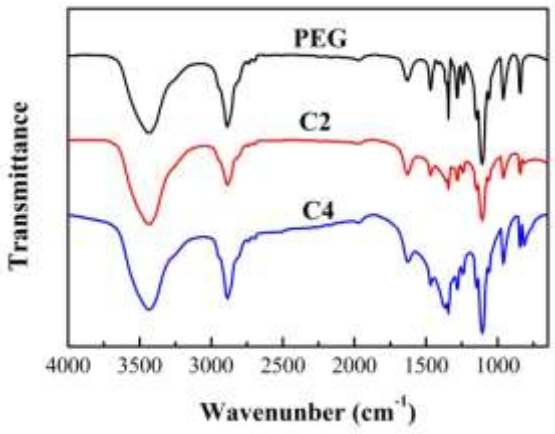

Fig. S11 FTIR spectrum of PEG, C2 and C4.